

---

# Neuromorphic Random Walk for Experimental Phosphate Adsorption Modeling

---

**Rodrigo P. Ferreira**

Pritzker School of Molecular Engineering  
University of Chicago  
Chicago, IL, USA  
rpferreira@uchicago.edu

**Rui Ding**

Pritzker School of Molecular Engineering  
University of Chicago  
Chicago, IL, USA  
ruiding@uchicago.edu

**Rapti Ghosh**

Pritzker School of Molecular Engineering  
University of Chicago  
Chicago, IL, USA  
rapti@uchicago.edu

**Haihui Pu**

Pritzker School of Molecular Engineering  
University of Chicago  
Chicago, IL, USA  
haihuipu@uchicago.edu

**Junhong Chen**

Pritzker School of Molecular Engineering  
University of Chicago  
Chemical Sciences and Engineering Division  
Physical Sciences and Engineering Directorate  
Argonne National Laboratory  
Chicago, IL, USA  
junhongchen@uchicago.edu, junhongchen@anl.gov

## Abstract

Neuromorphic systems leverage their intrinsic parallelism and event-driven behavior to deliver energy-efficient and low-latency solutions. Although such advantages have been extensively demonstrated in proof-of-concept settings with synthetic data, evidence of high performance on real-world tasks remains scarce due to neuromorphic systems' relatively low resolution. To address this gap, we apply an unsupervised neuromorphic random walk (NRW) algorithm to experimental data from phosphate adsorption on multiple remote-gate electrodes. Our model autonomously segments sensor dynamics into regimes that agree with the underlying adsorption theory, with a strong fit ( $R^2 > 0.98$ ) with the traditional pseudo-second-order (PSO) kinetics model used in this case. Using the Langmuir model, the NRW also predicts consistent Gibbs free energy values for this process. This work provides an initial step towards a theory-consistent and practical NRW deployment, enabling more efficient and noise-resilient sensing platforms.

## 1 Introduction

Despite recent advances in edge-sensing devices, many machine learning (ML) pipelines still rely on offline (cloud) processing without any verification against physics models [1, 2]. This leads to high latency issues and waste of resources (*e.g.*, time, energy) while providing physically inconsistent estimates—motivating on-chip computation and integrated physics checks into the pipeline [1–3].

As one of the most promising platforms for edge solutions, neuromorphic computing (NMC) has been making substantial progress from a mathematical and proof-of-concept standpoint, showing provable advantages across many tasks [4, 5]. However, real-world demonstrations remain rare due to limitations in model accuracy, signal resolution, and robustness under noisy conditions [4, 5].

We propose that a neuromorphic random walk (NRW) pipeline is a promising way to address both problems. On one hand, random walks are ubiquitous across multiple physics-based and numerical computing tasks via Monte Carlo methods [6]. On the other hand, NRW’s energy advantage and competitive latency have been formally demonstrated as well [4, 5, 7].

The main contribution of this work is to provide a physics-consistent, cross-device phosphate adsorption modeling pipeline. We apply NRW to real experimental data, and validate the predicted adsorption segment (regime) with standard physics models, demonstrating robust, noise-resilient performance, and competitive accuracy.

Specifically, we collect experimental data—transfer curve of field-effect transistor (FET) sensors—observed in different phosphate concentrations and across multiple remote-gate electrodes on various substrates; further details provided in sub-section 2.1. Bayesian inference criterion (BIC) [8] is applied to the sensing data to determine the number of states ( $k^*$ ) that best describe the underlying physicochemical events. Given the sensing time-series and  $k^*$ , the NRW algorithm correctly segments the sensing signal into sections that agree with physics-based models for phosphate adsorption, from both kinetic and thermodynamic perspectives.

In this paper, we describe the basic principles of NMC, NRW, and our experimental setup (section 2), followed by our results and discussion (section 3).

## 2 Methodology

### 2.1 Experimental setup and data

The experiments have been conducted across different phosphate concentrations: a few in the pg/mL, ng/mL concentration range, and the remaining being 1  $\mu\text{g}/\text{mL}$ , 10  $\mu\text{g}/\text{mL}$ , 20  $\mu\text{g}/\text{mL}$ , 1 mg/mL, and 2 mg/mL. Since most instances [18–21] of our benchmark models—to be discussed in sub-section 2.3—do not apply to extremely low or high phosphate concentrations, we have focused on 1  $\mu\text{g}/\text{mL}$ , 10  $\mu\text{g}/\text{mL}$ , 20  $\mu\text{g}/\text{mL}$ , and 1 mg/mL. The experiments have been conducted following standard and rigorous protocols from studies involving similar devices in the web lab [24–26].

The setup includes a diverse set of field-effect transistor (FET) devices. In addition to regular graphene substrate, we have aerosol jet printed cellulose nanocrystal (CNC)-graphene ink to produce a remote-gate electrode. There are also indium-tin-oxide polyethylene naphthalate and terephthalate (ITO-PEN and ITO-PET, respectively) substrates, which have been inkjet printed using ethyl cellulose (EC) graphene ink. It is worth mentioning that we have an annealing process with  $\text{N}_2$  flow for the silicon samples, whereas ITO-PEN and ITO-PET electrodes are subject to photonic annealing without  $\text{N}_2$  flow.

As for the collected data, we run each experiment across all phosphate concentrations and remote-gate electrodes. Each experiment is repeated 50 times (cycles), and each cycle consists of measuring both the current and voltage in the drain and gate components of the FET sensor, *i.e.*,  $I_d(t)$ ,  $I_g(t)$ ,  $V_d(t)$ ,  $V_g(t)$ [26]. The drain voltage remains at  $V_d = 50$  mV at all times, while the gate voltage  $V_g$  goes from 0 to 2 V with constant 50 mV increments. Thus, given the controlled voltage conditions, we use  $I_d(t)$  and  $I_g(t)$  as inputs to our NRW model. Figures 1 and 2 in the Appendix section illustrate an example of a 50-cycle transfer curve and the segmentation of the  $I_d(t)$ ,  $I_g(t)$  curves into three states, respectively.

### 2.2 Principles of neuromorphic computing

Drawing inspiration from the human brain, NMC is fundamentally different from its digital (von Neumann) counterpart on many levels [9]. Apart from spike versus binary data representation, other major differences include operation (parallel or sequential) and organization (co-located or separated memory and processing units). Moreover, while digital processors are time-driven (synchronous), neuromorphic processors are event-driven (asynchronous)—a major feature that has been leveraged to build energy-efficient computing platforms [9].

The building block of NMC is the neuron model. This work uses the leaky-integrate-and-fire (LIF) neuron due to its simplicity and accuracy. The LIF model approximates the neuron to a low-pass filter circuit made of a resistor  $R$  and a capacitor  $C$ —which is valid from a biological standpoint [9]. Mathematically, the neuron’s membrane potential  $U(t)$  evolves over time as

$$\tau \frac{dU(t)}{dt} = -U(t) + RI(t), \quad (1)$$

where  $\tau = RC$  is the circuit’s time constant, and  $I(t)$  is the current flowing through the circuit at any given time  $t$ . Assuming  $I(t)$  constant and defining the decay rate as  $\beta = e^{-1/\tau}$ , Eq.(1) solution is  $U(t) = RI + (U_0 - RI)\beta^t$ . The discrete-time version of this solution then becomes  $U_t = \beta U_{t-1} + R(1 - \beta)I_t$ .

A practical way to understand this solution is that the membrane potential increases whenever a spike arrives at the neuron, while simultaneously decaying over time according to its  $\beta$  factor [9]. At any given time, if the membrane potential reaches the threshold value  $\theta$ , the neuron fires a spike to its neighbors and the potential resets to zero.

### 2.3 Neuromorphic random walk and validation

Random walks naturally match the underlying physics of adsorption-desorption on surfaces [10–12], enabling complete kinetic modeling through continuous-time Markov chain jumps between “free” and “adsorbed” states, for example [12, 13]. Our NRW solution starts by taking the raw sensing time-series ( $I_d(t)$ ,  $I_g(t)$ ), and applying a BIC to determine the best number  $k^*$  of sufficiently distinct states that can be observed in our temporal data. To do so, we use a Savitzky-Golay filter [14] to lightly smooth and stabilize the derivatives of the signal.

The feature vector  $\vec{x}_t$  is defined as

$$\vec{x}_t = [\log_{10}(\dot{I}_d(t)), \log_{10}(\dot{I}_g(t)), \log_{10}(\max(I_d(t)))] , \quad (2)$$

where  $\max(I_d(t))$  is the maximum  $I_d(t)$  value up until the time instant  $t$  within that given cycle, and  $\dot{I}_d(t)$ ,  $\dot{I}_g(t)$  are the first derivatives of  $I_d(t)$  and  $I_g(t)$ , respectively. The motivation for this specific definition comes from the inspection of a typical  $I_d(t)$  and  $I_g(t)$  behavior over a cycle.

Having defined the feature vector, the BIC algorithm is executed for multiple values of  $k$ —specifically,  $2 \leq k \leq 10, k \in \mathbb{Z}$ —to determine which one is associated with the lowest score ( $k^*$ ). On top of the regular BIC score, there is a penalty to account for singleton states, *i.e.*, states made of just one data point. The rationale is that such states could have a low BIC score (suggesting a good solution), but lack of any physical meaning in practical terms. The singleton-penalty correction allows us to achieve the best solution from both a clustering and physics perspective, leading to  $k^* = 3$ .

The next step consists of using  $I_d(t)$ ,  $I_g(t)$ ,  $k^*$  as inputs to the NRW model. It consists of a three-LIF neuron pool—also known as winner-take-all (WTA) spike [15]—that “votes” which state label (0, 1, or 2) should be assigned to each time step. This is achieved through a lateral inhibition mechanism, which is essentially an adaptation of Eq. (1) that forces that only one neuron will fire. Mathematically,

$$\tau \dot{v}_k = -(v_k - V_{\text{rest}}) + RI_k - g_{\text{inh}} \sum_{j \neq k} s_j, \quad (3)$$

where  $s_k = 1$  if  $v_k \geq V_\theta$ , and zero otherwise. As a result, the WTA spike results in a single label per time step, given by  $z_t = \arg \max_k s_{k,t}$ , in a one-hot encoding framework. Since we are dealing with  $k^* = 3$  states, we have  $z_t \in \{0, 1, 2\}$ .

The same procedure is repeated for all time steps to count the number of transitions between states. For each pair of states  $(i, j)$ , the number of transitions  $i \rightarrow j$  is divided by the total number of transitions across all states to get  $a_{ij}$ —the corresponding element in the transition matrix  $A \in \mathbb{R}^{3 \times 3}$ .

This process generates data on the population of each state as a function of time, enabling the Gaussian emission density calculation [16] for a given state  $j$  as  $e_{j,t} = N(x_t | \mu_j, \sigma_j)$ , which is the multivariate normal (Gaussian) density of the feature vector  $x_t$  under state  $j$ , with mean  $\mu_j$  and covariance  $\sigma_j$ . The motivation for this is to define a data likelihood score, *i.e.*, how typical a given feature vector  $\vec{x}_t$  is for a certain state  $j$ .

Combining the emission density  $e_{j,t}$  with the Markov prior  $p_t$  [17]:

$$\tilde{p}_t = A^T p_{t-1}, p_t = \frac{e_t \odot \tilde{p}_t}{\mathbf{1}^T (e_t \odot \tilde{p}_t)}, \quad (4)$$

produces data-aligned posteriors and corrects the curve segmentation into three states. Finally,  $\hat{z}_t = \arg \max_k (p_t(k))$  is measured to get the correct label for a given time step, resulting in a string of characters 0, 1, 2 per cycle.

To objectively verify whether the NRW has correctly labeled the states, we rely on the vast literature on phosphate adsorption. From a kinetic perspective, pseudo-first-order (PFO) and pseudo-second-order (PSO) are the main models that match phosphate behavior [18, 19], given by  $q(t) = q_e(1 - e^{-k_1 t})$  and  $q(t) = \frac{q_e^2 k_2 t}{1 + q_e k_2 t}$ , respectively. In other words, if we correctly identify the adsorption states, this specific curve segment should match the PSO model with high accuracy—and a bit lower for the PFO model, as suggested by the literature [18, 19].

Finally, we make a thermodynamics-based argument to further validate the NRW results. By combining the PSO fitting data and the Langmuir isotherm  $q_e = q_{\max} K C / (1 + K C)$  [20, 21], we can also fit this curve with our predicted adsorption segment and estimate the constant  $K$ . We then make it dimensionless via  $K^0 = K \times (1 \text{ mol/L})$ , and compute the Gibbs free energy as  $\Delta G^0 = -RT \ln K^0$ , with  $T = 298.15 \text{ K}$ , and  $R = 8.314 \text{ J/(mol.K)}$ —which shall be compared to common phosphate adsorption values in the literature, namely  $-20 \text{ kJ/mol} \leq \Delta G^0 \leq -10 \text{ kJ/mol}$  [22, 23].

### 3 Results and discussion

Table 1 contains the results of the analysis described in section 2. All results have been obtained in a simulation environment, using Python and the snnTorch package [9]. We also include the  $R^2$  fit results for PSO via a traditional approach in Python using a hard-coded 3-state hidden Markov model (3S-HMM) as a benchmark.

It is worth noting that due to our main focus on neuromorphic methods and strict page limits, we have not reported results obtained via traditional random walk methods. Although such methods could, in principle, achieve similar results to NRW, previous publications [4, 5] suggest that the power consumption would still be much lower for the latter. Given our downstream application focus on edge sensing devices, the NRW approach becomes the optimal solution.

As we can see in Table 1, NRW-derived  $R^2$  values for the PFO model are similar to those reported in the literature [18], ranging from 0.60 to 0.71, approximately. Conversely, PSO-related  $R^2$  results are much higher (from 0.96 to 0.99) and also agree with traditional python calculations using the hmmlearn package. This result is physically-consistent because the reaction rate is usually governed by surface reactions (*e.g.*, inner-sphere complexation) and multi-step uptake. Thus, PSO can track this behavior and remaining-capacity dependence more faithfully than PFO—a better fit for describing early external-mass-transfer control [18, 19].

Additionally, the estimated values for  $\Delta G^0$  are also consistent with the literature [22, 23]. As a spontaneous reaction across all substrates, all results are indeed negative. The range is also reasonable given reported values from  $-20 \text{ kJ/mol}$  to  $-10 \text{ kJ/mol}$ . One can observe a relatively high standard deviation in such  $\Delta G^0$  calculations, which is likely due to an admittedly small number of experiments and the high complexity of FET devices (with multiple components interacting with one another).

In summary, we have presented a physics-consistent, cross-device NRW algorithm operating on real phosphate adsorption experimental data. With a physics-informed prior (number of states  $k^*$ ), NRW accurately segments the sensing signals and infers the adsorption regime, as validated via the PSO kinetics model and the Langmuir isotherm. Such results match traditional offline calculations (*e.g.*, HMM), while being designed for energy-efficient edge deployment. Thus, it addresses two main gaps (*e.g.*, latency, physics-consistency) in current edge-sensing ML pipelines.

As for the next steps, we will run additional random walk methods that do not require physics-embedded components, such as the number of states  $k^*$ . We are also interested in expanding this framework to other ions, aiming to ultimately build a sensor matrix for multiple adsorption models. More importantly, we plan to deploy the NRW on real neuromorphic processors (*e.g.*, Intel Loihi) to quantify energy and latency gains, while enabling on-chip inference within a noise-resilient platform—a crucial step towards real-time edge-sensing applications.

Table 1: NRW results across all concentrations (1  $\mu\text{g/mL}$ , 10  $\mu\text{g/mL}$ , 20  $\mu\text{g/mL}$ , 1 mg/mL) and substrates (graphene, ITO-PEN, ITO-PET, Si-SiO<sub>2</sub>), including the  $R^2$  fit value for both PFO, PSO, and  $\Delta G^0$  via the Langmuir model. All results have been obtained in a simulation environment using Python.

	1 $\mu\text{g/mL}$	10 $\mu\text{g/mL}$	20 $\mu\text{g/mL}$	1 mg/mL
Graphene				
R <sup>2</sup> PFO (NRW)	0.704	0.714	0.662	0.594
R <sup>2</sup> PSO (NRW)	0.980	0.981	0.982	0.979
R <sup>2</sup> PSO (3S-HMM)	0.967	0.984	0.975	0.983
$\Delta G^0$ (kJ/mol)	-15.3 ± 4.4	-16.8 ± 4.2	-17.6 ± 4.1	-14.2 ± 3.3
ITO-PEN				
R <sup>2</sup> PFO (NRW)	0.600	0.596	0.595	0.605
R <sup>2</sup> PSO (NRW)	0.984	0.987	0.988	0.988
R <sup>2</sup> PSO (3S-HMM)	0.982	0.979	0.980	0.988
$\Delta G^0$ (kJ/mol)	-14.1 ± 3.4	-15.1 ± 5.2	-15.0 ± 4.3	-13.3 ± 2.6
ITO-PET				
R <sup>2</sup> PFO (NRW)	0.709	0.731	0.720	0.602
R <sup>2</sup> PSO (NRW)	0.977	0.977	0.978	0.984
R <sup>2</sup> PSO (3S-HMM)	0.978	0.979	0.978	0.981
$\Delta G^0$ (kJ/mol)	-16.0 ± 3.9	-15.8 ± 3.8	-15.3 ± 3.4	-15.1 ± 3.6
Si-SiO <sub>2</sub>				
R <sup>2</sup> PFO (NRW)	0.715	0.711	0.711	0.613
R <sup>2</sup> PSO (NRW)	0.975	0.976	0.977	0.983
R <sup>2</sup> PSO (3S-HMM)	0.979	0.976	0.969	0.984
$\Delta G^0$ (kJ/mol)	-16.4 ± 4.2	-15.9 ± 3.6	-16.4 ± 3.6	-14.9 ± 3.4

## Acknowledgments and Disclosure of Funding

This research was supported by multiple institutional and federal grants. This project is supported by the Eric and Wendy Schmidt AI in Science Postdoctoral Fellowship, a Schmidt Sciences, LLC program. This work was also in part supported by the National Science Foundation Future Manufacturing Project #2037026. Additional support came from the University of Chicago Data Science Institute through the 2024 AI+Science Research Initiative. We acknowledge the Carbon High-Performance Computing Cluster at the Center for Nanoscale Materials, Argonne National Laboratory, supported by the U.S. Department of Energy Office of Science User Facility under Contract No. DE-AC02-06CH11357. We declare no conflict of interest for this work.

## A Appendix: Experimental Data

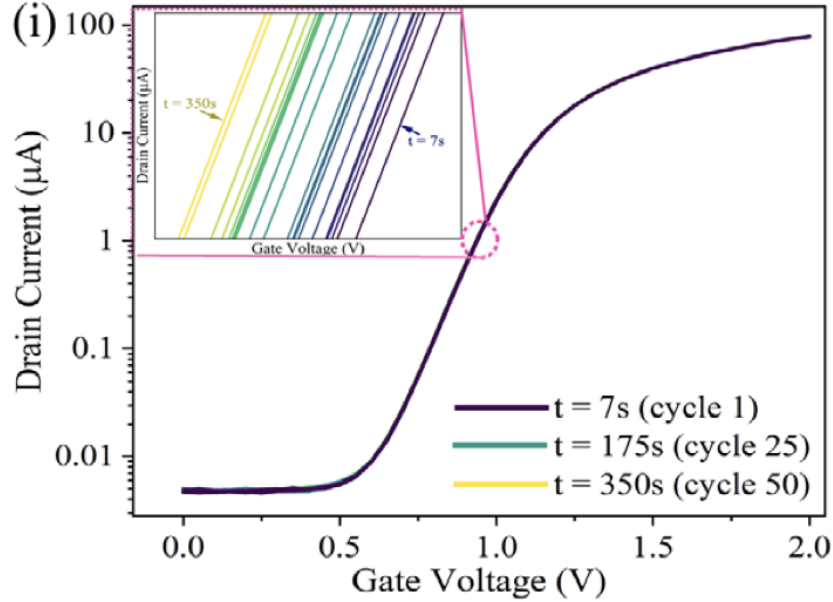


Figure 1: Schematic of the 50 cycles transfer curve that changes over different stages of the analyte reaction with the sensor probe. Adapted from [26].

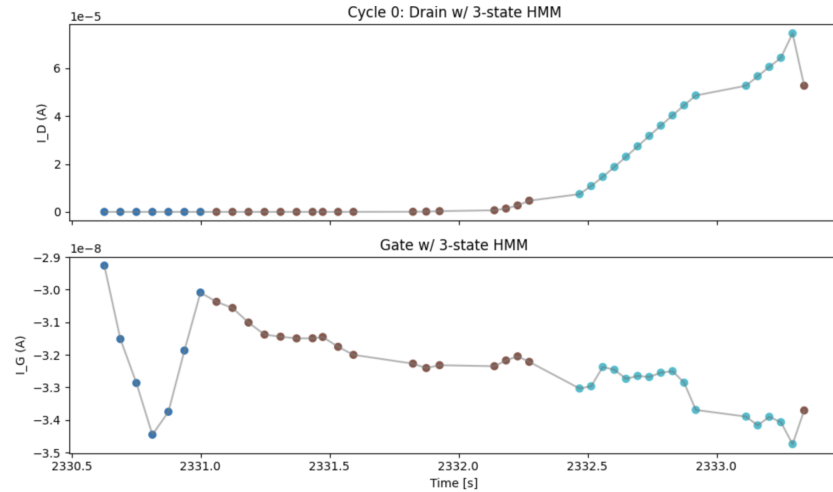


Figure 2: Sample plot illustrating the curve segmentation for drain and gate current over time ( $I_d(t)$ ,  $I_g(t)$ ) through a 3-state HMM approach. Each specific color of points (dark blue, brown, light blue) corresponds to a distinct state identified by the model.

## References

- [1] Singh, Raghbir, and Sukhpal Singh Gill. "Edge AI: a survey." *Internet of Things and Cyber-Physical Systems* 3 (2023): 71-92.
- [2] Wang, Xubin, and Weijia Jia. "Optimizing edge AI: a comprehensive survey on data, model, and system strategies." *arXiv preprint arXiv:2501.03265* (2025).
- [3] Karniadakis, George Em, Ioannis G. Kevrekidis, Lu Lu, Paris Perdikaris, Sifan Wang, and Liu Yang. "Physics-informed machine learning." *Nature Reviews Physics* 3, no. 6 (2021): 422-440.
- [4] Aimone, James B., Prasanna Date, Gabriel A. Fonseca-Guerra, Kathleen E. Hamilton, Kyle Henke, Bill Kay, Garrett T. Kenyon et al. "A review of non-cognitive applications for neuromorphic computing." *Neuromorphic Computing and Engineering* 2, no. 3 (2022): 032003.
- [5] Smith, J. Darby, Aaron J. Hill, Leah E. Reeder, Brian C. Franke, Richard B. Lehoucq, Ojas Parekh, William Severa, and James B. Aimone. "Neuromorphic scaling advantages for energy-efficient random walk computations." *Nature Electronics* 5, no. 2 (2022): 102-112.
- [6] Rathore, Nitin, and Juan J. de Pablo. "Monte Carlo simulation of proteins through a random walk in energy space." *The Journal of chemical physics* 116, no. 16 (2002): 7225-7230.
- [7] Theilman, Bradley H., and James B. Aimone. "Solving Sparse Finite Element Problems on Neuromorphic Hardware." *arXiv preprint arXiv:2501.10526* (2025).
- [8] Neath, Andrew A., and Joseph E. Cavanaugh. "The Bayesian information criterion: background, derivation, and applications." *Wiley Interdisciplinary Reviews: Computational Statistics* 4, no. 2 (2012): 199-203.
- [9] Eshraghian, Jason K., Max Ward, Emre O. Neftci, Xinxin Wang, Gregor Lenz, Girish Dwivedi, Mohammed Bennamoun, Doo Seok Jeong, and Wei D. Lu. "Training spiking neural networks using lessons from deep learning." *Proceedings of the IEEE* 111, no. 9 (2023): 1016-1054.
- [10] Chew, Wei-Xiang, Kazunari Kaizu, Masaki Watabe, Sithi V. Muniandy, Koichi Takahashi, and Satya NV Arjunan. "Surface reaction-diffusion kinetics on lattice at the microscopic scale." *Physical Review E* 99, no. 4 (2019): 042411.
- [11] Mercado, Enrique, Hyun Tae Jung, Changho Kim, Alejandro L. Garcia, Andy J. Nonaka, and John B. Bell. "Surface coverage dynamics for reversible dissociative adsorption on finite linear lattices." *The Journal of Chemical Physics* 159, no. 14 (2023).
- [12] Andersen, Mie, Chiara Panosetti, and Karsten Reuter. "A practical guide to surface kinetic Monte Carlo simulations." *Frontiers in chemistry* 7 (2019): 202.
- [13] Ulissi, Zachary W., Jingqing Zhang, Ardemis A. Boghossian, Nigel F. Reuel, Steven FE Shimizu, Richard D. Braatz, and Michael S. Strano. "Applicability of birth-death markov modeling for single-molecule counting using single-walled carbon nanotube fluorescent sensor arrays." *The Journal of Physical Chemistry Letters* 2, no. 14 (2011): 1690-1694.
- [14] Krishnan, Sunder Ram, and Chandra Sekhar Seelamantula. "On the selection of optimum Savitzky-Golay filters." *IEEE transactions on signal processing* 61, no. 2 (2012): 380-391.
- [15] Wang, Di, Rui Feng Tang, Huai Lin, Long Liu, Nuo Xu, Yan Sun, Xuefeng Zhao et al. "Spintronic leaky-integrate-fire spiking neurons with self-reset and winner-takes-all for neuromorphic computing." *Nature Communications* 14, no. 1 (2023): 1068.
- [16] Zhuang, Xinhua, Yan Huang, Kannappan Palaniappan, and Yunxin Zhao. "Gaussian mixture density modeling, decomposition, and applications." *IEEE Transactions on Image Processing* 5, no. 9 (1996): 1293-1302.
- [17] Rabiner, Lawrence R. "A tutorial on hidden Markov models and selected applications in speech recognition." *Proceedings of the IEEE* 77, no. 2 (2002): 257-286.

- [18] Luo, Xin, Xiurong Wang, Shaopan Bao, Xiawei Liu, Weicheng Zhang, and Tao Fang. "Adsorption of phosphate in water using one-step synthesized zirconium-loaded reduced graphene oxide." *Scientific reports* 6, no. 1 (2016): 39108.
- [19] Mao, Yanpeng, and Qinyan Yue. "Kinetic modeling of phosphate adsorption by preformed and in situ formed hydrous ferric oxides at circumneutral pH." *Scientific reports* 6, no. 1 (2016): 35292.
- [20] Marczewski, Adam W. "Analysis of kinetic Langmuir model. Part I: integrated kinetic Langmuir equation (IKL): a new complete analytical solution of the Langmuir rate equation." *Langmuir* 26, no. 19 (2010): 15229-15238.
- [21] Holford, I. C. R., R. W. M. Wedderburn, and G. E. G. Mattingly. "A Langmuir two-surface equation as a model for phosphate adsorption by soils." *Journal of Soil Science* 25, no. 2 (1974): 242-255.
- [22] Kalaitzidou, Kyriaki, Anastasios Zouboulis, and Manassis Mitrakas. "Thermodynamic study of phosphate adsorption and removal from water using iron oxyhydroxides." *Water* 14, no. 7 (2022): 1163.
- [23] Yoon, Seo-Young, Chang-Gu Lee, Jeong-Ann Park, Jae-Hyun Kim, Song-Bae Kim, Sang-Hyup Lee, and Jae-Woo Choi. "Kinetic, equilibrium and thermodynamic studies for phosphate adsorption to magnetic iron oxide nanoparticles." *Chemical engineering journal* 236 (2014): 341-347.
- [24] Jang, Hyun-June, Hyou-Arm Joung, Artem Goncharov, Anastasia Gant Kanegusuku, Clarence W. Chan, Kiang-Teck Jerry Yeo, Wen Zhuang, Aydogan Ozcan, and Junhong Chen. "Deep learning-based kinetic analysis in paper-based analytical cartridges integrated with field-effect transistors." *ACS nano* 18, no. 36 (2024): 24792-24802.
- [25] Jang, Hyun-June, Rapti Ghosh, Wen Zhuang, Xiaoben Zhang, Yuqin Wang, Xiaoao Shi, Xingkang Huang et al. "Fine Tuning of Electrical Characteristics of Inkjet Printed Graphene for Physical and Chemical Sensing." *ACS applied materials & interfaces* 17, no. 8 (2025): 12911-12920.
- [26] Ghosh, Rapti, Fengxue Zhang, Hyun-June Jang, Janan Hui, Kayla Vittore, Haoyang You, Rozyyev Vepa et al. "Real-Time Phosphate Monitoring via Plant-Derived Graphene Ink FET Sensors Integrated with Deep Learning." *Energy & Environmental Materials* (2025): e70144.